Magnetic Resonance Materials in Physics, Biology and Medicine
https://doi.org/10.1007/s10334-024-01205-3

RESEARCH ARTICLE

Real-time automated quality control for quantitative MRI

Andrew Dupuis[1] · **Rasim Boyacioglu**[2] · **Kathryn E. Keenan**[3] · **Mark A. Griswold**[1,2]

Received: 31 May 2024 / Revised: 31 August 2024 / Accepted: 17 September 2024

Abstract

Objective This work presents an automated quality control (QC) system within quantitative MRI (qMRI) workflows. By leveraging the ISMRM/NIST quantitative MRI system phantom, we establish an open-source pipeline for rapid, repeatable, and accurate validation and stability tracking of sequence quantification performance across diverse clinical settings.

Materials and methods A microservice-based QC system for automated vial segmentation from quantitative maps was developed and tested across various MRF acquisition and protocol designs, with reports generated and returned to the scanner in real time.

Results The system demonstrated consistent and repeatable value segmentation and reporting, successfully extracted all 252 T1 and T2 vial samples tested. Values extracted from the same sequence were found to be repeatable with 0.09% ± 1.23% and – 0.26% ± 2.68% intersession error, respectively.

Discussion By providing real-time quantification performance assessment, this easily deployable automated QC approach streamlines sequence validation and long-term performance monitoring, vital for the broader acceptance of qMRI as a standard component of clinical protocols.

Keywords Magnetic resonance fingerprinting · Automated quality control · Quantitative MRI · Image processing · Performance monitoring · ISMRM/NIST system phantom

Introduction

Magnetic resonance fingerprinting (MRF) is a well-established approach to quantitative magnetic resonance imaging (qMRI), enabling simultaneous acquisition and multi-parametric characterization of biological tissues [1]. Since its inception, MRF has shown the potential to revolutionize the landscape of clinical imaging by providing a rapid and detailed assessment of tissues, which is pivotal in the diagnosis and management of various pathologies [2–4]. Despite its proven efficacy and versatility, the translation of MRF from a research setting into routine clinical practice necessitates rigorous and consistent quality control (QC) protocols. The intricacy of MRF sequences and the sensitivity of the technique to hardware and software variations underscore the need for robust QC measures to ensure accurate and reliable imaging across different clinical environments [5–7] and as scanner hardware or software evolves [8–10].

The challenge lies in the fact that qMRI, and by extension MRF, implementations often lack a standardized and automated framework for quality assurance. Traditional QC methods for MRI [7, 11], which typically involve visual validation of image quality, are largely inadequate for quantitative MRI [7, 11]. While automated tools for phantom value segmentation exist [12], there remains a need for scanner-integrated QC systems capable of providing real-time, accurate assessments of sequence quantification performance. Responding to this need, we present an online, automated QC framework tailored for qMRI applications. Utilizing the National Institute of Standards and Technology (NIST) and the International Society for Magnetic Resonance in Medicine (ISMRM) system phantom [13], we propose a standardized and objective means to assess the in vitro performance of qMRI sequences. The choice of the

✉ Andrew Dupuis
andrew.dupuis@case.edu

[1] Department of Biomedical Engineering, Case Western Reserve University, Cleveland, OH, USA

[2] Department of Radiology, Case Western Reserve University, Cleveland, OH, USA

[3] Physical Measurement Laboratory, National Institute of Standards and Technology, Boulder, CO, USA

Published online: 03 October 2024

ISMRM/NIST phantom reflects its commercial availability and designed emulation of a range of human tissue magnetic properties, providing a reliable benchmark for calibration and performance evaluation [5, 14].

The core of the proposed system is a containerized computational environment that encapsulates the QC process, facilitating deployment across various computational infrastructures while ensuring consistency and reproducibility. This approach aligns with the emerging trends in medical software development, where containerization plays a critical role in achieving computational reproducibility [15], scalability [16], and decentralization [17]. In addition, the system is integrated with a cloud-based logging mechanism that stores detailed site-, hardware-, and sequence-specific logs of sequence performance, enabling long-term monitoring and analysis of performance.

This study uses image recognition algorithms to automate the segmentation of quantitative values from the vials within the ISMRM/NIST phantom. Such automation can significantly reduce the human error in QC processes [12, 18–20] and contributes to the reproducibility of the system. Moreover, the automatic generation and feedback of Digital Imaging and Communications in Medicine (DICOM®) compatible reports directly to the scanner console ensures that the QC results are immediately accessible in a human-readable format, facilitating prompt decision-making regarding sequence suitability or validity on the day of the test. Such a system should not only streamline the validation process of research sequences but also enhance the traceability of clinical results.

Materials and methods

The proposed automated quality control system consists of integration between the acquisition system, reconstruction environment, and containerized QC daemon. Figure 1 demonstrates the proposed system's data flow: raw data was acquired on the scanner and streamed in real-time via the Framework for Image Reconstruction Environment [21] (FIRE) interface prototype to a remote reconstruction server. Resulting maps were piped to a QC daemon for vial segmentation, analysis, and report generation, with reports comparing reconstructions against NIST reference values appended and returned to the scanner console via FIRE alongside the quantitative maps. In addition, performance metrics can be logged to the cloud provider's blob storage service according to site information, scanner hardware details and high-level sequence specifications extracted from the raw data.

Acquisition infrastructure and protocol

Acquisitions were primarily performed using a high-level interpreter supporting user-provided sequence definitions (mrftools [22]) and compatible with FIRE [21] for raw data emission. Alternatively, if evaluating an existing imaging protocol for which vendor-provided reconstructions are available, the resulting maps can also be sent as image data via a FIRE "add-in" module.

If evaluating a 2D acquisition method, following a standard localization scan, the operator selects slice positions parallel to and centered on the T1/$NiCl_2$ and T2/$MnCl_2$ reference layers, respectively,—2D layers can be evaluated

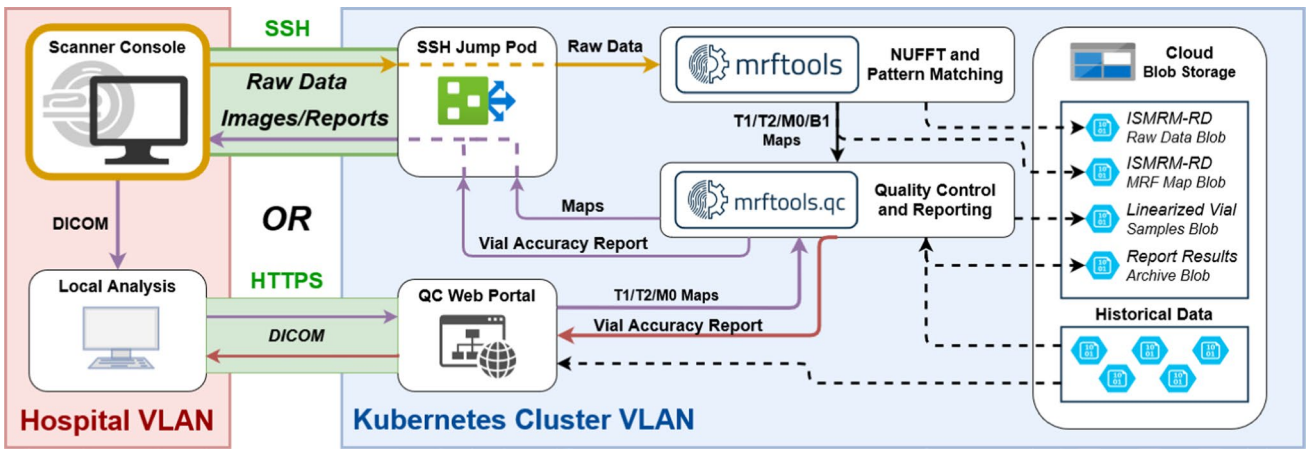

Fig. 1 Automated quality control system architecture: schematic representation of the automated quality control (QC) system architecture for magnetic resonance fingerprinting (MRF). This diagram illustrates the comprehensive workflow from data acquisition on the scanner, real-time streaming to a remote reconstruction server, analysis by the QC daemon, and report generation. The automated process ensures real-time, accurate assessment of sequence performance against NIST reference values, facilitating immediate quality control decisions

individually or in aggregate. If evaluating a 3D acquisition method, the operator selects a slice plane parallel to and centered on the T2/$MnCl_2$ reference layer as the center of the imaging volume, ensuring that the imaging field of view adequately covers both reference vial layers. Slice thickness must be less than 0.5x the diameter of the target vials. Due to limitations of the MRF protocols used for system evaluation in this manuscript, the ISMRM/NIST phantom was positioned such that the T1/$NiCl_2$ and T2/$MnCl_2$ reference layers could be imaged with axial rather than coronal slices, with the anterior/posterior axis of the phantom (as described in the phantom's user documentation) oriented along the magnet's bore. The described vial identification system requires neither full coverage of the phantom nor positioning at isocenter, so long as any evaluated image planes align parallel to the evaluated reference layer(s).

Reconstruction environment

If raw data are provided to the reconstruction system, processing is performed within Docker containers on a secure Kubernetes cluster hosted by a public cloud provider. Source code for container generation and Helm/Kubernetes-based deployment are provided in the data availability statement, but all containers used are also compatible with other orchestration environments. Raw data were uploaded via a Secure Shell (SSH) connection between the scanner's host computer and an ingress jump node within the reconstruction cluster. Metadata associated with the incoming connection allows the ingress node to facilitate a connection between the scanner and the appropriate reconstruction pod. Given that reconstruction design governs a substantial portion of an MRF experiment, the reconstruction cluster supports JSON-based pipeline definitions as a raw data sidecar, allowing for dynamic configuration of the processing pipeline.

In the case that vendor-reconstructed quantitative maps were provided to the system rather than raw data, images and requisite metadata was piped through a reconstruction "dummy" pod for reformatting and tagging with metadata needed by the QC daemon pod.

Image processing and vial segmentation

The online QC infrastructure proposed is agnostic to the vial segmentation approach used. For example, atlas-based methods have been proposed for the phantom used in this study [12], albeit with limitations on image dimensionality and resolution. The modular containerized approach specified in this work is amenable to extension and modification with alternative mask generation approaches without compromising the remainder of the system's architecture.

While convolution-based vial detection is commonly used for fiducial spheres with uniform and fixed contrast characteristics [13], such approaches struggle when vial image contrast varies or is poorly determined, such as in 2D single-slice data featuring only the T1 and T2 evaluation vials. In this study, an image processing approach was implemented using Canny edge detection [23] followed by Hough transformation [24] to identify circular regions of the appropriate pixel size as governed by the phantom's vial specifications and the incoming image data's field of view and matrix dimensions (see Fig. 2).

Image preprocessing

1. **Normalization:** Incoming MRF datasets, comprising T1, T2, and M0 maps, undergo a normalization process to convert the multi-parametric data into a grayscale image for subsequent processing to enhance the contrast and visibility of features (e.g., vials) within the images. This involves normalizing by the maximum M0 value within the slice and assigning normalized T1, T2, and M0 values to the red, green, and blue color channels of an RGB32 image which is then converted to grayscale according to the ITU BT.601 luminance equation [25]:

$$Y = 0.299 * R + 0.587 * G + 0.114 * B, \quad (1)$$

where Y is the resulting grayscale intensity of a voxel. This process creates a luminance space driven by a combined representation of T1, T2, and M0 to improve circle detection across a range of contrast conditions.
2. **Edge enhancement:** the Canny edge detection algorithm is applied on the normalized luminance space to isolate edges within the resulting grayscale images. By emphasizing the boundaries between vials and the surrounding medium, this step significantly improves the efficacy of the subsequent Hough transform in detecting circular features.
3. **Hough transformation:** the circular Hough transform works by scanning the edge-enhanced image for points that could belong to the perimeter of a circle with any radius within the specified range. For each edge point detected in the preprocessing stage, the algorithm computes a circle for every possible radius and increments the accumulator space corresponding to the center of these circles. This process effectively votes for the center and radius of potential circles. The accumulator space, therefore, represents a grid where each cell's value indicates the number of edge points that suggest a circle with a specific center and radius. After processing all edge points, the algorithm examines this accumulator space to identify local maxima-cells with values exceeding a predetermined detection threshold.

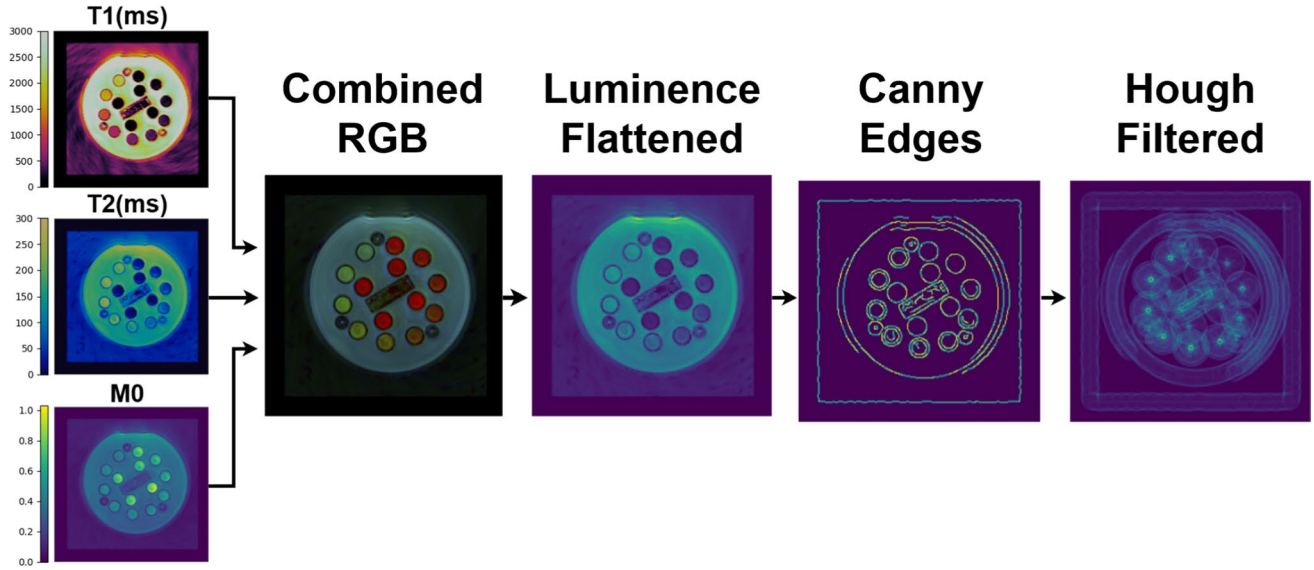

Fig. 2 Image processing and vial segmentation workflow: detailed workflow of the image processing and vial segmentation process within the automated QC pipeline. Starting with normalization and edge enhancement for enhanced feature visibility, the application of Canny edge detection and Hough transformation for identifying circular vials in MRF datasets is demonstrated

These maxima correspond to the circles' parameters (center coordinates and radii) that were most frequently indicated by the edge points. A range of expected radii is calculated based on the physical dimensions of the vials (corresponding to expected circular features) and the imaging resolution from the raw data (ISMRM-RD [26]) or image data (DICOM®) header. The detection threshold plays a crucial role in distinguishing between true circles present in the MRI slices by determining the minimum number of votes (i.e., edge points agreeing on a specific circle's parameters) required for a potential circle to be considered a true detection.

4. **Deduplication and overlap correction:** given that overlapping features or image ringing can also be detected as multiple circles, a merging step is performed on the Hough transformation results to consolidate closely aligned features into single entities. Circles are merged based on both proximity and radius similarity, with adjustable thresholds defined in the user-configurable settings.

Region validation and identification

Validation ensures that detected features accurately represent the intended physical objects within the MRI slices. The intent behind these validation steps is twofold: to eliminate outlier detections that do not correspond to real vials (thus improving the specificity of the analysis) and to ensure that the system's analysis matches the physical phantom's design. Each detected circle is evaluated to ensure it maintains a realistic proximity to other circles, reflective of the expected physical arrangement of vials within the phantom in real-world units (millimeters) to assess distances accurately. Given the symmetrical design of the chosen system phantom, a distance criterion is applied where all circles must be within the expected range from at least two other circles to be considered valid based on the known spatial distribution of vials within the phantom.

Once circles have been validated, the system classifies the MRI slice layers according to the detected tissue properties, distinguishing between T1/$NiCl_2$, T2/$MnCl_2$, and Proton Density (PD)/D20 layers. This classification relies on comparing the statistical analysis of tissue properties within the detected circles against predefined reference values and patterns. PD layers are identified by their uniformity of T1/T2 values across all detected circles within a slice. For non-PD layers, a pattern matching algorithm using mean squared error (MSE) was implemented to compare the detected patterns of tissue properties with predefined reference patterns. For each T1/T2 layer detected with the appropriate number of total vials in valid positions, the mean value of each detected vial is extracted. The resulting list is then sorted in ascending order, and the pattern of T1/T2 values is pattern-matched against the sorted list of anticipated T1/T2 vial values from the reference specification, resulting in a layer classification. If the analysis of tissue properties matches the reference patterns for T1 or T2 relaxation times, the layer is classified accordingly. Layers that do not meet the criteria for T1, T2, or PD classification are considered non-specific or invalid for the purposes of relaxation property analysis.

After vial segmentation, the resulting masks were then applied to the unmodified T1 and T2 maps to generate buffers of T1 and T2 values for each detected region, sorted in ascending order by regional means. These buffers were then passed to the reporting function for evaluation, DICOM® generation, and persistent logging.

DICOM®-based reports and cloud logging

The reporting function accepts incoming labeled buffers of voxel T1 and T2 values for each vial, along with metadata specifying the acquisition site, scanner hardware, and acquisition sequence used. First, the mean and standard deviation of each vial's T1 and T2 samples were calculated and plotted versus the corresponding NIST reference values using matplotlib [27]. Plots were then converted to greyscale, blitted to unsigned integer pixel arrays, and returned as ISMRM-RD image data to the original reconstruction process that called the QC daemon for appending to the quantitative maps sent back to the acquisition system. In addition, the complete voxel data from each vial is stored as Numpy [28] arrays to site-, hardware-, and sequence-specific blob storage assets corresponding to the date and time of the acquisition. The stored voxel buffers and metadata allow for longitudinal intra-configuration or inter-configuration comparisons of sequence, reconstruction, and hardware performance in a retrospective manner.

Containerized DICOM® web interface

In order to call the QC pipeline on existing exported DICOM® datasets, a simple web interface was created as a microservice for deployment as a secondary pod associated with the QC daemon. The web interface supports the upload of properly tagged DICOM® datasets with associated DICOMDIR metadata in compressed forms (zip, tar.gz). Uploaded datasets are extracted to the expected format by the web interface microservice, then passed to the QC daemon pod via a persistent volume within the cluster. Resulting reports and raw extraction data are available as downloadable files once processing is completed. An example of the web interface can be found in Fig. 3.

Evaluation and performance

To evaluate the performance of the proposed automated qMRI QC pipeline, 3D-MRF acquisitions were performed on a clinical 3T MRI scanner (Siemens, VA50A, Vida 3T) using two different MRF acquisition designs acquired three times each across two very different slice thicknesses (2 mm and 5 mm). As the focus of this manuscript is the QC pipeline rather than the acquisition parameters, the pipeline was evaluated by

1. The total percentage of successful vial segmentation (defined as the ratio of vials for which data were extracted properly versus the total number of vials for which data were acquired).
2. The intraclass correlation coefficient (ICC) for T1 and T2 values for sequence and vials across sessions.
3. Bland–Altman plots across all tested sequences and vials for all paired measurement interleaves.

Results

A total of 9 3D-MRF datasets were acquired with field-of-view coverage of both the T1/$NiCl_2$ and T2/$MnCl_2$ reference layers, each of which contains 14 target vials, corresponding to a total of 252 vial samples. Of these imaged vials, the proposed QC system successfully extracted all 252, and corresponding online-generated vial segmentation reports for all imaging volumes are available in the supplementary material. An example report for one $NiCl_2$ layer, reformatted for readability of each section, can be found in Fig. 4.

Figure 5 demonstrates the repeatability of vial value segmentations across both layers for all three sequences, with a mean ICC greater than 0.999. In addition, a Bland–Altman plot of the percent difference between test/retest pairs was prepared in Fig. 6. T1 and T2 values extracted from the same sequence were found to be repeatable with $0.09\% \pm 1.23\%$ and $-0.26\% \pm 2.68\%$ intersession error, respectively.

Discussion

The implementation of an automated QC system for qMRI represents a step towards improved traceability of both precision and accuracy across scanners and through time. By integrating distributed software architecture with real-time data analysis, our approach paves the way for broader clinical adoption of qMRI modalities through improved standardization and trust. The containerized QC system presented in this work ensures consistent execution environments, mitigating issues arising from hardware and software heterogeneity—particularly in multi-center studies—which is vital for ensuring that the QC process is unaffected by external variables. The modular design of the system allows for traceable integration of new algorithms or updates to existing ones. Such flexibility is crucial in a rapidly evolving field like MRF, where frequent sequence updates are necessary to keep pace with technological advancements and emerging clinical needs.

The system successfully handled multiple MRF sequences and slice thicknesses, validating its practicality for deployment across diverse clinical settings. Vial values were automatically detected at runtime and were found to be

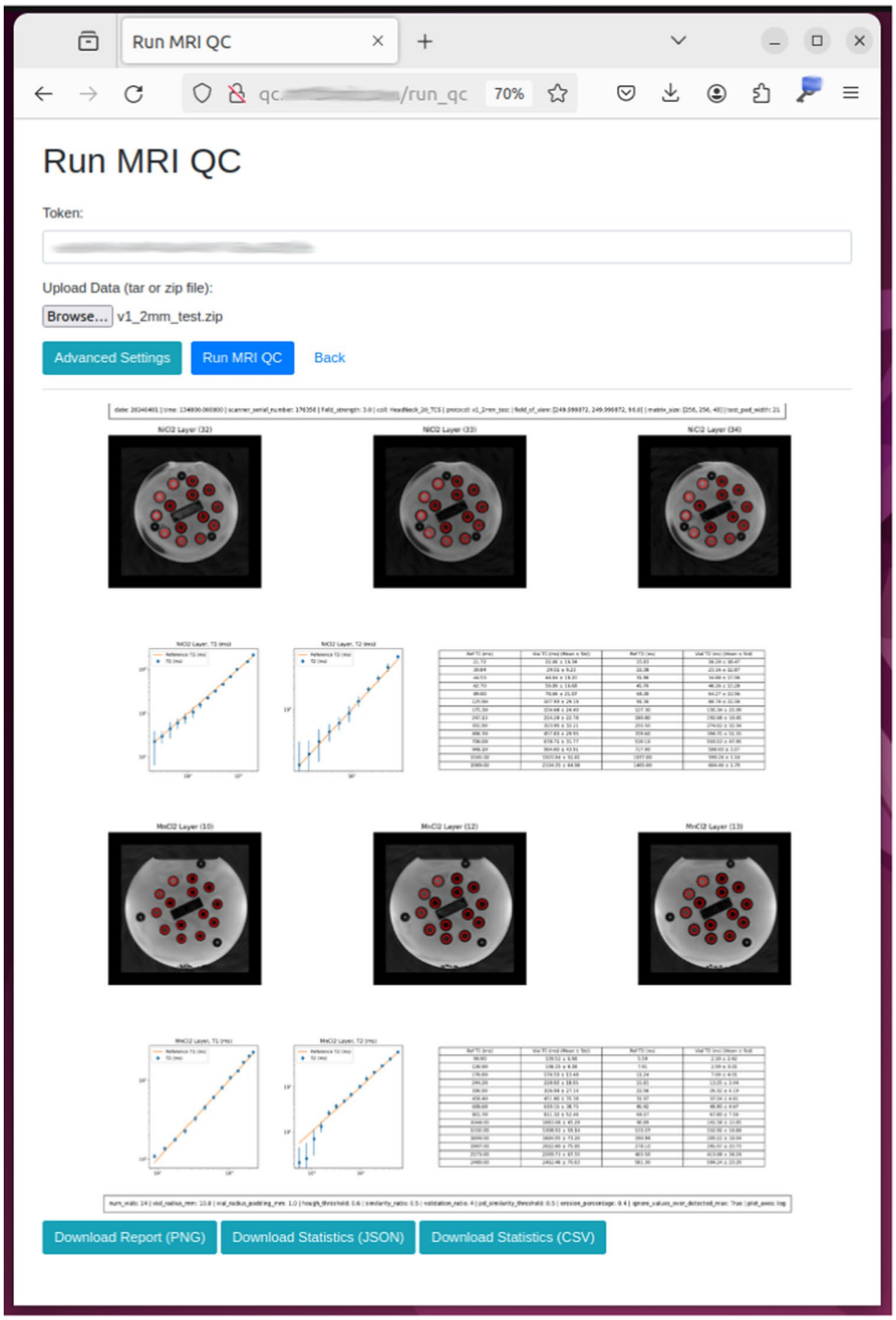

Fig. 3 DICOM®-compatible web interface: a web interface is provided supporting the upload and automated evaluation of DICOMDIR-structured image datasets commonly exported from vendor scanner interfaces. The image-based report as well as CSV or JSON structured vial data can be downloaded directly from the web interface after processing via the same daemon as the real-time reporting pipeline

repeatable across different sequences and slice thicknesses, with repeatability metrics at or below the thermal stability of the phantom [13], despite the lack of temperature control during these evaluations. Although this study focused on validating the QC pipeline in a controlled single-scanner environment, the results are transferable based on prior findings [6] demonstrating that automated segmentation methods used in 3D-MRF can be highly robust across different scanners, subjects, and sessions, with minimal variation observed between different hardware. Dupuis et al. (2024) showed that MRF data, when acquired and processed through a standardized pipeline, maintained consistency across multiple scanner models, suggesting that the robustness observed in a single-scanner context can be expected to hold across different platforms. This indicates that while our study focused on single-scanner

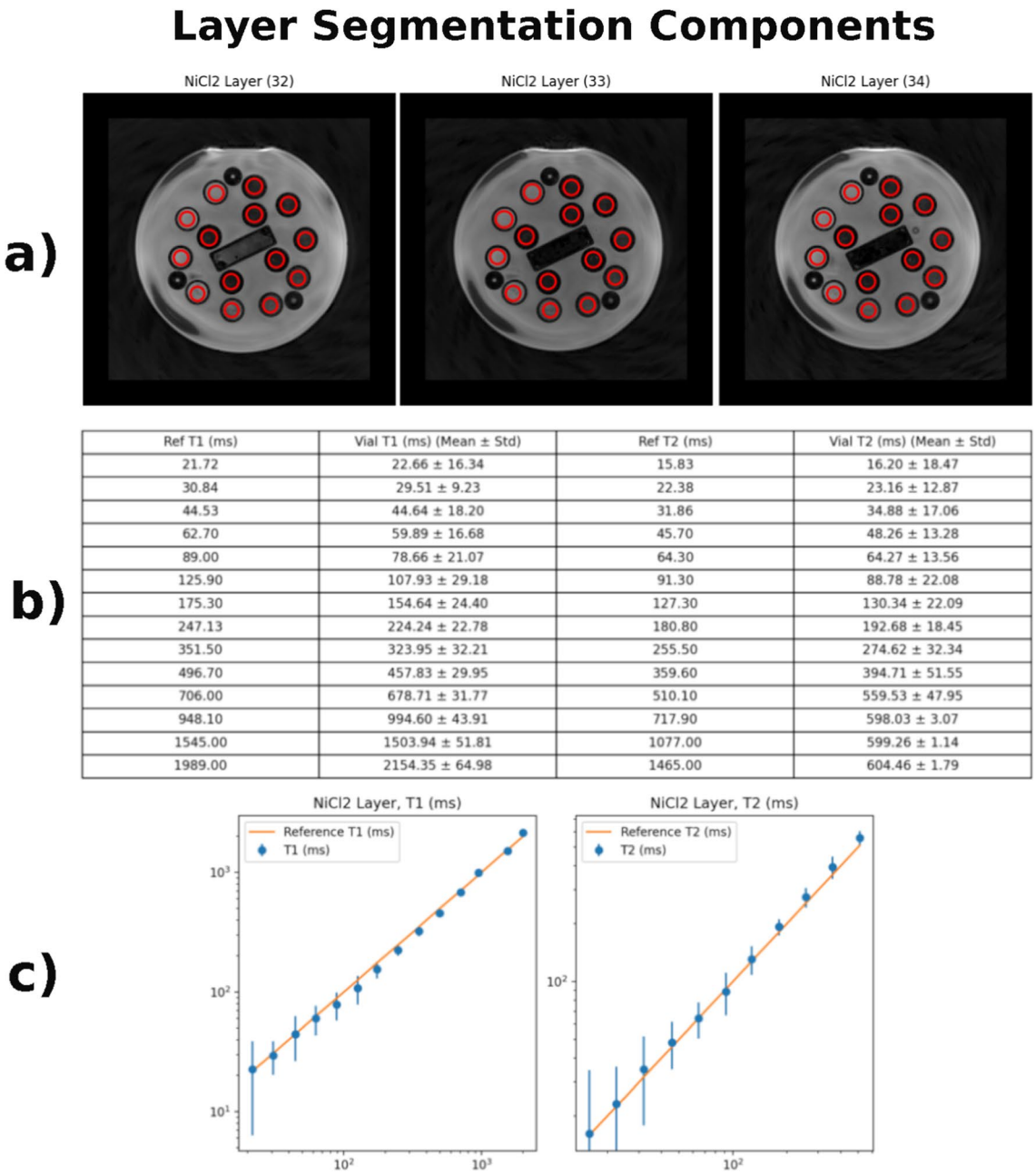

Ref T1 (ms)	Vial T1 (ms) (Mean ± Std)	Ref T2 (ms)	Vial T2 (ms) (Mean ± Std)
21.72	22.66 ± 16.34	15.83	16.20 ± 18.47
30.84	29.51 ± 9.23	22.38	23.16 ± 12.87
44.53	44.64 ± 18.20	31.86	34.88 ± 17.06
62.70	59.89 ± 16.68	45.70	48.26 ± 13.28
89.00	78.66 ± 21.07	64.30	64.27 ± 13.56
125.90	107.93 ± 29.18	91.30	88.78 ± 22.08
175.30	154.64 ± 24.40	127.30	130.34 ± 22.09
247.13	224.24 ± 22.78	180.80	192.68 ± 18.45
351.50	323.95 ± 32.21	255.50	274.62 ± 32.34
496.70	457.83 ± 29.95	359.60	394.71 ± 51.55
706.00	678.71 ± 31.77	510.10	559.53 ± 47.95
948.10	994.60 ± 43.91	717.90	598.03 ± 3.07
1545.00	1503.94 ± 51.81	1077.00	599.26 ± 1.14
1989.00	2154.35 ± 64.98	1465.00	604.46 ± 1.79

Fig. 4 Vial segmentation report components: the three components of each automated segmentation and analysis report for T1 and T2 vials for each layer of an ISMRM/NIST phantom. The top sections (**a**) display MRI slices with overlaid red circles indicating the successful identification of vials. The middle sections (**b**) are tables that present the quantitative T1 and T2 values extracted from the vials. The bottom section (**c**) plot the detected values against reference values to assess the accuracy of the sequence

tests to emphasize system effectiveness for longitudinal comparisons, the principles underlying our QC system are applicable across a multi-scanner deployment.

As can be seen in Fig. 5, substantial deviations (~10%) can be observed in certain vials with very short T1 or T2 values. This can largely be attributed to encoding and sensitivity limits of the sequences tested in vials outside of the physiological ranges for which the examined sequences were optimized, rather than the QC method itself. These vials demonstrate the benefits of a robust QC system in assessing the repeatability and highlighting performance limits of a particular sequence design.

The QC system's potential usefulness extends beyond immediate deployment to optimizing quantitative imaging protocols and identifying biases in different processing pipelines. By leveraging the longitudinal datasets archived

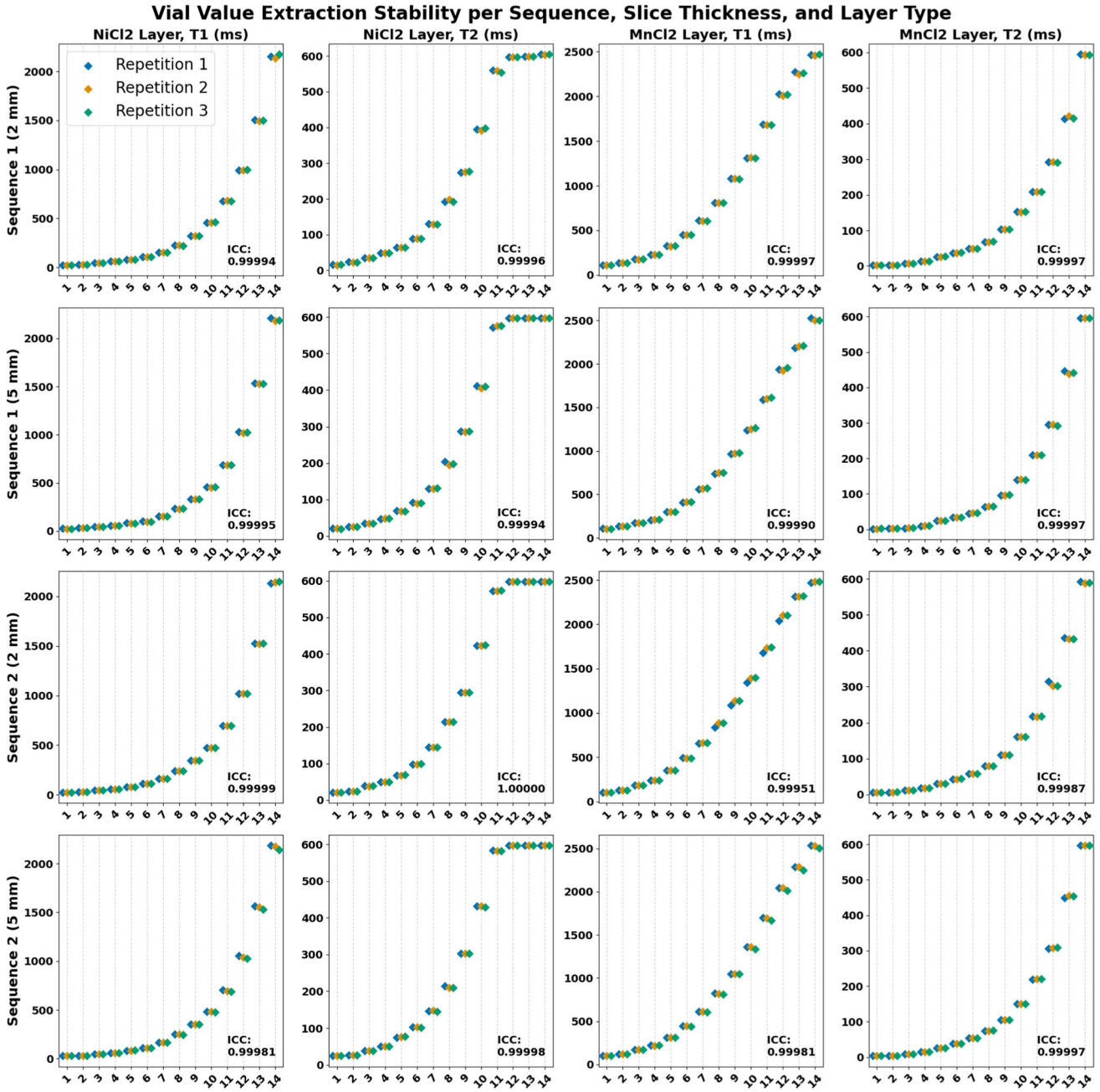

Fig. 5 Intraclass correlation coefficient (ICC) analysis: visualization of the intraclass correlation coefficient (ICC) analysis across vials for test–retest reliability of T1 and T2 measurements within the ISMRM/NIST phantom across multiple MRF acquisitions. The plots display the T1 and T2 values for the initial test and two retests, with an ICC of 1.0 indicating identical reproducibility across tests. This demonstrates both the consistency of the MRF technique in capturing the relaxation properties of the phantom's vials, as well as the vial segmentation system's consistency

within the system—whether stored locally or in cloud-based platforms like Azure Blob storage—automation of optimization processes becomes feasible. Currently, the QC system does not directly support longitudinal analyses from the scanner or web interface due to the variety of study designs and reporting structures that may be desired across studies. However, the system facilitates these analyses by offering downloadable CSV and JSON packages that integrate date, sequence structure, and other relevant metadata that allows for easy parsing and direct application to various longitudinal study designs. Results can also be archived to Azure Blob storage in real time, providing a secure and scalable solution for managing large datasets over extended periods. Finally, the modular

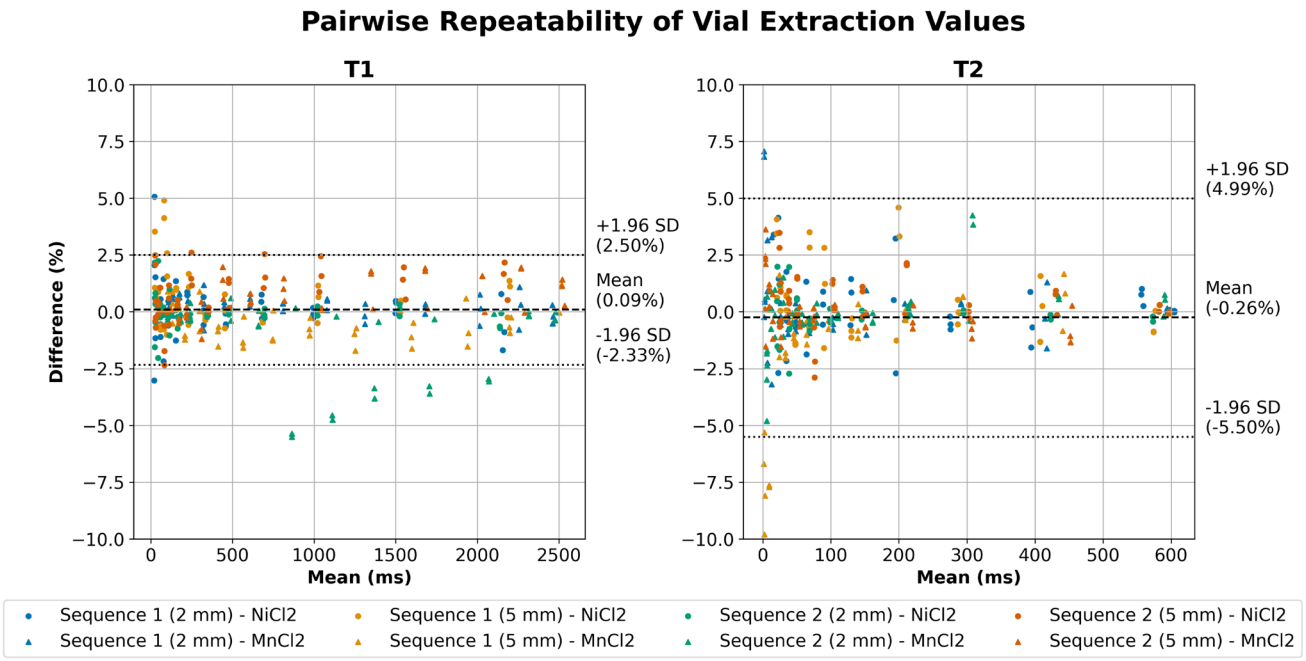

Fig. 6 Bland–Altman Plot for test–retest reliability: Bland–Altman plots demonstrating intersession repeatability of T1 and T2 vial segmentation values for various magnetic resonance fingerprinting (MRF) acquisitions. The plots compare the percent differences between paired measurements from multiple MRF sequences against the sample pair mean values, with the mean difference and limits of agreement (±1.96 SD) indicated. The compact clustering of points around the mean difference lines for both T1 and T2 measurements highlights the reliable repeatability and consistency of the automated QC system over successive sessions

structure and persistent volume claim architecture also allows for easy creation of study-specific custom "report" modules for installation within the same Helm chart and direct reporting to the scanner via the same infrastructure described.

The feasibility of deploying the QC system across different vendor setups is reinforced by its reliance on vendor-independent data standards such as DICOM and ISMRM-RD streams. The web interface operates with standard DICOM files, allowing for flexibility in automated data identification by customizing tags used for T1, T2, M0, etc., maps. The user-exposed web-based interface allows for adjustment of vial detection parameters on-the-fly without code modifications in scenarios where vial segmentation fails for unanticipated or system-specific reasons. In addition, the web interface is easily extensible—future work includes the addition of phantom serial number input to dynamically configure the detection algorithm and reference values based on the phantom's hardware version. Regarding the system's adaptability to alternate sequences, the pipeline's design allows for straightforward customization. To adapt the software to different MRF sequences or processing pipelines, modifications are primarily confined to the configuration files, specifically the JSON settings sidecar, where DICOM tags for T1, T2, and M0 (or PD) images are specified. Provided these images are available and co-registered, the system can accommodate any sequence design.

For technologists and medical physicists, the immediate feedback provided by an online QC system enables rapid detection and response to changes in scan performances. The system's interface, including features like the on-scanner QC evaluation checkbox and web daemon support, ensures that it can be seamlessly integrated into existing clinical QC workflows. Containerized and orchestrated pipelines such as proposed in this work allow for easy deployment on a local system or via integration into existing high-performance computing clusters. Support for SSH additionally allows for low-barrier, secure integration with clinical systems via vendor tools such as FIRE. For clinicians, the long-term data aggregation capability of the system also opens up new avenues for clinical research, with improved traceability and provable system stability potentially allowing improved data aggregation for retrospective studies and protocol optimization.

The proposed automated QC system enhances traceability in qMRI acquisition and reconstruction by capturing and logging high-level sequence specifications, reconstruction parameters, and performance metrics. This framework allows for precise correlation between technical choices and quantification outcomes, significantly aiding in the optimization of parameters for specific applications

and troubleshooting issues on novel or malfunctioning hardware. Such record-keeping not only facilitates long-term performance monitoring but also sheds light on the stability and repeatability of scanner hardware over time. Importantly, longitudinal QC data can reveal hardware performance trends that may not be apparent in shorter studies, contributing to the development of more reliable qMRI systems. Moreover, system-specific data become invaluable for validating sequences, particularly following scanner hardware or software upgrades, as it simplifies the process of identifying any deviations in performance.

Supplementary Information The online version contains supplementary material available at https://doi.org/10.1007/s10334-024-01205-3.

Data availability The software described in this work is available under an academic research license via Zenodo [29] (https://doi.org/10.5281/zenodo.11115989). All validation datasets in DICOM format are available via Zenodo [30] (https://doi.org/10.5281/zenodo.11372539).

Declarations

Conflict of interest A. Dupuis, R. Boyacioglu, and M. Griswold receive research support from Siemens Healthineers. M. Griswold has MRF patents licensed by Siemens.

Ethical approval Not applicable.

Consent to participate Not applicable.

References

1. Ma D, Gulani V, Seiberlich N, Liu K, Sunshine JL, Duerk JL, Griswold AM (2013) Magnetic resonance fingerprinting. Nature 495:187–92
2. Chen Y, Chen MH, Baluyot KR, Potts TM, Jimenez J, Lin W (2019) Mr fingerprinting enables quantitative measures of brain tissue relaxation times and myelin water fraction in the first five years of life. Neuroimage 186:782–793. https://doi.org/10.1016/j.neuroimage.2018.11.038
3. MacAskill CJ, Markley M, Farr S, Parsons A, Perino JR, McBennett K, Kutney K, Drumm ML, Pritts N, Griswold MA, Ma D, Dell KM, Flask CA, Chen Y (2021) Rapid b1-insensitive mr fingerprinting for quantitative kidney imaging. Radiology 300:380–387. https://doi.org/10.1148/RADIOL.2021202302
4. Ontaneda D, Gulani V, Deshmane A, Shah A, Guruprakash DK, Jiang Y, Ma D, Fisher E, Rudick RA, Raza P, Kilbane M, Cohen JA, Sakaie K, Lowe MJ, Griswold MA, Nakamura K, Magnetic resonance fingerprinting in multiple sclerosis, Multiple Scler Related Disord 79. https://doi.org/10.1016/j.msard.2023.105024
5. Jiang Y, Ma D, Keenan KE, Stupic KF, Gulani V, Griswold MA (2017) Repeatability of magnetic resonance fingerprinting t1 and t2 estimates assessed using the ismrm/nist mri system phantom. Magn Resonan Med 78:1452–1457. https://doi.org/10.1002/MRM.26509
6. Dupuis A, Chen Y, Hansen M, Chow K, Sun JEP, Badve C, Ma D, Griswold MA, Boyacioglu R, Quantifying 3d mr fingerprinting (3d-mrf) reproducibility across subjects, sessions, and scanners automatically using mni atlases, Magn Reson Med https://doi.org/10.1002/mrm.29983
7. Keenan KE, Biller JR, Delfino JG, Boss MA, Does MD, Evelhoch JL, Griswold MA, Gunter JL, Hinks RS, Hoffman SW, Kim G, Lattanzi R, Li X, Marinelli L, Metzger GJ, Mukherjee P, Nordstrom RJ, Peskin AP, Perez E, Russek SE, Sahiner B, Serkova N, Shukla-Dave A, Steckner M, Stupic KF, Wilmes LJ, Wu HH, Zhang H, Jackson EF, Sullivan DC (2019) Recommendations towards standards for quantitative mri (qmri) and outstanding needs. J Magn Reson Imaging 49:e26–e39. https://doi.org/10.1002/jmri.26598
8. Keenan KE, Gimbutas Z, Dienstfrey A, Stupic KF (2019) Assessing effects of scanner upgrades for clinical studies. J Magn Reson Imaging 50:1948–1954. https://doi.org/10.1002/jmri.26785
9. Karakuzu A, Biswas L, Cohen-Adad J, Stikov N (2022) Vendor-neutral sequences and fully transparent workflows improve inter-vendor reproducibility of quantitative mri. Magn Reson Med 88:1212–1228. https://doi.org/10.1002/MRM.29292
10. Dupuis A, Chen Y, Griswold MA, Boyacioglu R, Quantifying repeatability of a 3d-mrf protocol during scanner software upgrades. In: ISMRM Annual Meeting
11. Cashmore MT, McCann AJ, Wastling SJ, McGrath C, Thornton J, Hall MG (2021) Clinical quantitative mri and the need for metrology. Br J Radiol 94:20201215. https://doi.org/10.1259/BJR.20201215/FORMAT/EPUB
12. Korte JC, Chin Z, Carr M, Holloway L, Franich R, Magnetic resonance biomarker assessment software (mr-bias): an automated open-source tool for the ismrm/nist system phantom. Phys Med Biol 68. https://doi.org/10.1088/1361-6560/acbcbb
13. Stupic KF, Ainslie M, Boss MA, Charles C, Dienstfrey AM, Evelhoch JL, Finn P, Gimbutas Z, Gunter JL, Hill DL, Jack CR, Jackson EF, Karaulanov T, Keenan KE, Liu G, Martin MN, Prasad PV, Rentz NS, Yuan C, Russek SE (2021) A standard system phantom for magnetic resonance imaging . https://doi.org/10.1002/mrm.28779
14. Keenan KE, Gimbutas Z, Dienstfrey A, Stupic KF, Boss MA, Russek SE, Chenevert TL, Prasad PV, Guo J, Reddick WE, Cecil KM, Shukla-Dave A, Nunez DA, Konar AS, Liu MZ, Jambawalikar SR, Schwartz LH, Zheng J, Hu P, Jackson EF, Multi-site, multi-platform comparison of mri t1 measurement using the system phantom. PLoS One 16. https://doi.org/10.1371/JOURNAL.PONE.0252966
15. Moreau D, Wiebels K, Boettiger C Containers for computational reproducibility. Nat Rev Methods Primers 3. https://doi.org/10.1038/s43586-023-00236-9
16. Huo Y, Blaber J, Damon SM, Boyd BD, Bao S, Parvathaneni P, Noguera CB, Chaganti S, Nath V, Greer JM, Lyu I, French WR, Newton AT, Rogers BP, Landman BA (2018) Towards portable large-scale image processing with high-performance computing. https://doi.org/10.1007/s10278-018-0080-0
17. Kim Y, Joshi AA, Choi S, Joshi SH, Bhushan C, Varadarajan D, Haldar JP, Leahy RM, Shattuck DW Brainsuite bids app: Containerized workflows for mri analysis, Preprint. bioRxiv https://doi.org/10.1101/2023.03.14.532686
18. Gedamu EL, Collins DL, Arnold DL (2008) Automated quality control of brain mr images. J Magn Reson Imaging 28:308–319. https://doi.org/10.1002/jmri.21434
19. Sun J, Barnes M, Dowling J, Menk F, Stanwell P, Greer PB (2015) An open source automatic quality assurance (osaqa) tool for the acr mri phantom. Australas Phys Eng Sci Med 38:39–46. https://doi.org/10.1007/s13246-014-0311-8
20. Yang K, Saab D (2020) An intelligent analysis framework for clinical-translational mri research
21. Chow K, Kellman P, XH Prototyping image reconstruction and analysis with fire. In: SCMR 24th annual scientific sessions

22. Dupuis A, Bolding R, Chen Y, Boyacioglu R, Griswold MA (2024) mrftools: a research framework for integrated design, simulation, acquisition, and reconstruction of magnetic resonance fingerprinting (mrf) . https://doi.org/10.5281/zenodo.10479682
23. Canny J (1986) A computational approach to edge detection
24. Hough PV (1959) Machine analysis of bubble chamber pictures. In: International Conference on high energy accelerators and instrumentation, CERN 1959:554–556
25. International Telecommunication Union, Bt.601: Studio encoding parameters of digital television for standard 4:3 and wide screen 16:9 aspect ratios, International Telecommunication Union, accessed: Insert date here (n.d.)
26. Inati SJ, Naegele JD, Zwart NR, Roopchansingh V, Lizak MJ, Hansen DC, Liu CY, Atkinson D, Kellman P, Kozerke S, Xue H, Campbell-Washburn AE, Sørensen TS, Hansen MS (2017) Ismrm raw data format: a proposed standard for mri raw datasets. Magn Reson Med 77:411–421. https://doi.org/10.1002/mrm.26089
27. Hunter JD (2007) Matplotlib: a 2d graphics environment. Comput Sci Eng 9:90–95. https://doi.org/10.1109/MCSE.2007.55
28. Harris CR, Millman KJ, van der Walt SJ, Gommers R, Virtanen P, Cournapeau D, Wieser E, Taylor J, Berg S, Smith NJ, Kern R, Picus M, Hoyer S, van Kerkwijk MH, Brett M, Haldane A, del Río JF, Wiebe M, Peterson P, Gérard-Marchant P, Sheppard K, Reddy T, Weckesser W, Abbasi H, Gohlke C, Oliphant TE (2020) Array programming with numpy. Nature 585:357–362. https://doi.org/10.1038/s41586-020-2649-2
29. Dupuis A, Boyacioglu R, Yong C, Griswold M (2024) Code for real-time automated quality control for magnetic resonance fingerprinting. https://doi.org/10.5281/zenodo.11115989
30. Dupuis A, Griswold M, Boyacioglu R, Keenan K (2024) Magnetic resonance fingerprinting DICOM validation datasets for real-time automated quality control for quantitative MRI. https://doi.org/10.5281/zenodo.11372539